

All-Season Passive Thermal Management Film with Multifunctionality for Efficient Radiative Cooling and Solar Heating

Tingni Wu, Kai Yin,* Yuchun He, Lingxiao Wang, Haonan Yu, Yin Huang, Ji-An Duan, and Christopher J. Arnusch



Cite This: *J. Phys. Chem. Lett.* 2025, 16, 3654–3663



Read Online

ACCESS |



Metrics & More



Article Recommendations



Supporting Information

ABSTRACT: Thermal radiation management is an important aspect of thermal engineering and plays a crucial role in various industrial and environmental applications. However, either cooling or heating devices alone can exacerbate all-season consumption during hot summers or cold winters. We have designed a dual-mode thermal management device that can switch modes by a pull-out method, with femtosecond laser-induced graphene (LIG) on the surface of a polyimide membrane as the heating surface and a SiO₂ hollow microsphere coating as the cooling surface. Due to the multi-interface reflection between SiO₂ hollow microspheres and air, high reflectivity (93%) and 97% thermal infrared emissivity can be obtained. Under a solar irradiation intensity of 75 J/cm², a temperature decrease of 6.3 °C can be realized. On the other hand, LIG can achieve an ultra-ambient temperature increase of 35 °C due to its excellent solar light absorption characteristics ($\epsilon \approx 97\%$) and high thermal conductivity. Temperature regulation can be achieved by switching heating and cooling modes, which shows great promise in agriculture and for food and goods preservation. Also, this design is expected to offer a new approach to energy efficient cooling and heating in architecture.



Buildings contribute to more than 30% of the total global final energy consumption, and much of this energy is utilized for cooling and heating purposes.^{1–3} Thermal management plays an important role in people's productive activities in the face of extreme weather. Reducing the use of energy is also beneficial for the environment, by reducing pollution and emissions while significantly reducing costs. Therefore, highly energy efficient buildings have emerged as a critical objective for sustainability, necessitating advances in scientific and technological innovation.⁴ Among all alternative energy sources, solar energy is by far the most abundant and cleanest option.^{5–7} Therefore, properly utilizing solar radiation is an ideal strategy for zero-energy outdoor thermal management.^{8,9}

Passive thermal management enabled by well-designed optical structures has garnered considerable attention recently due to the advantages of high efficiency and zero energy consumption.^{10–12} Various optical designs have been developed,¹³ including randomly distributed particle structures,¹⁴ organic multilayers,^{15,16} emissive metamaterials,¹⁷ photonic crystals,^{18,19} and inorganic multilayers.²⁰ Lin et al. developed an all-inorganic narrowband emitter that can achieve efficient solar reflectance and thermal emissivity for radiative cooling in hot and humid regions.²¹ Zhang et al. developed a micro- and nanostructured surface based on a photothermally ice-phobic metal organic framework, which reached 98% solar light absorption.²² Research on radiative cooling and solar heating has led to notable improvements in technical performance and profound scientific discoveries.^{23–36} In addition to static thermal management, materials such as Janus films that can

switch between heating and cooling modes in order to cope with variable environmental conditions are also drawing a lot of attention.^{37–39} A sandwich-structured Janus membrane for personal thermal management was fabricated by Yue et al. It switches infrared emissivity between the Cu nanowire layer (0.436) and cellulose@LDH layer (0.973).⁴⁰ Zhang et al. developed a Janus film for thermal management in building applications. This membrane features a switchable infrared emissivity between the ZnO nanorods embedded in cellulose (0.87) and the silver nanowire layer (0.43).⁴¹ However, the reported designs are usually complex and costly to manufacture. In particular, the narrow temperature regulation range due to sacrificed heating/cooling performance remains a key issue limiting practical applications. Laser-treated PTFE wetted with ethanol can change the solar transmittance, and this feature is utilized to achieve temperature regulation.⁴² Such studies of dissolution-switching thermal management modes are subject to limitations related to their application scenarios and the stability of the materials involved. Therefore, providing a facile preparation method for a switchable dual-mode thermal management film that is free from environmental constraints is imperative.

Received: February 11, 2025

Revised: March 18, 2025

Accepted: March 27, 2025

Published: April 4, 2025



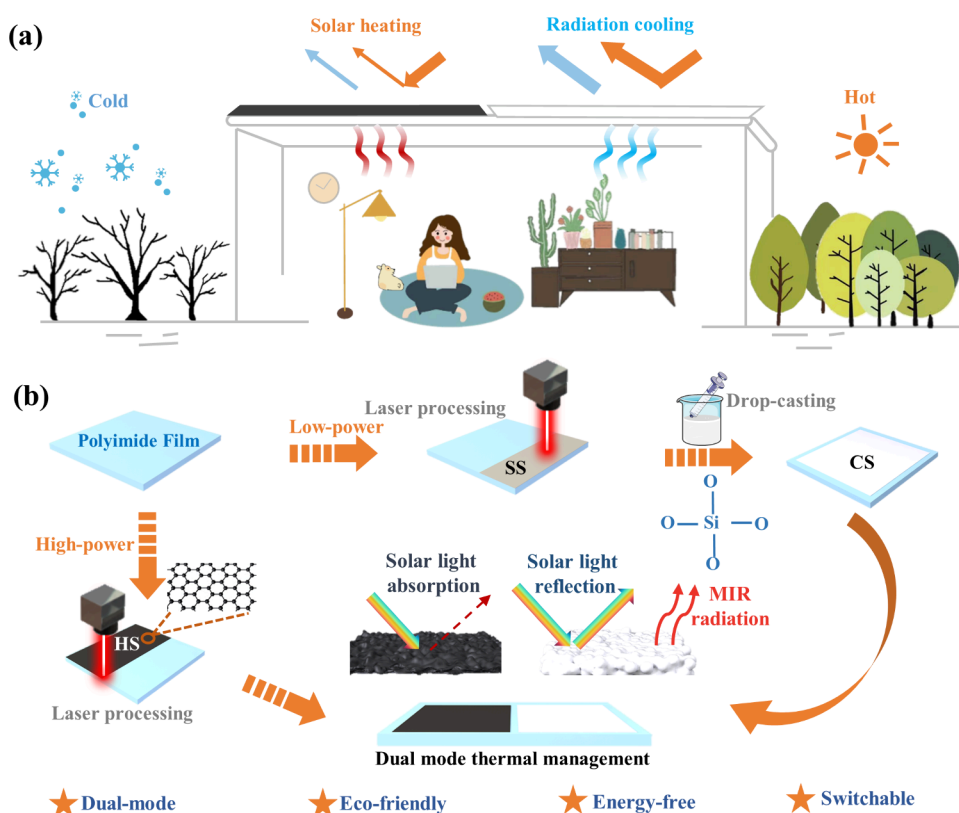


Figure 1. (a) Diagram illustrating the dual-mode device in its heating mode (left) and cooling mode (right). (b) Schematic of the preparation process of the dual-mode film.

In this work, we demonstrate a bimodal smart thermal management material. A superhydrophilic surface (SS) was prepared on the surface of a polyimide (PI) film by a femtosecond laser under low-power conditions. In this way, the SiO₂ mixture can be attached to the surface by drop-coating. Because of the optical properties of SiO₂, the cooling surfaces (CS) simultaneously possess high infrared emissivity ($\epsilon \sim 97\%$) and strong solar reflectivity ($R \sim 93\%$). Subsequently, the femtosecond laser under high-power conditions induced graphene as a heating surface (HS) on the PI surface with 97% solar absorption. Furthermore, a temperature decrease of 6.3 °C and a temperature increase of 35 °C compared with the sub-ambient temperature could be achieved in both modes. Meanwhile, the heating surface was explored to boost the germination of legume seeds at low temperatures. The cooling mode was also demonstrated in hot weather for its preservation effect on fruits. It is expected that such designs will not only lead to a promising new avenue for cooling and heating in energy-saving buildings but also have an impact in other fields such as seed germination and preservation of perishable goods.

As shown in Figure 1a, the dual-mode thermal management film consists of a thin film polymer composite with solar heating and radiative cooling capabilities side by side. The inherent molecular vibration modes of SiO₂ cause a high mid-infrared emissivity in the mid-infrared band. Therefore, it has excellent passive radiative cooling performance and can result in sub-ambient cooling. With respect to the heating mode, the temperature increase is mainly realized by solar radiation to heat conversion. The femtosecond laser has been advantageously used in various fields in recent years because of the high-precision, noncontact processing of substrates, combined

with high efficiency and environmental friendliness.^{43–52}

Figure 1b exhibits the fabrication process of the thermal management dual-mode film. At a low femtosecond laser power, line-by-line scanning of the hydrophilic untreated PI (UTPI) film resulted in a superhydrophilic surface (Figure S1). Water droplets on the UTPI surface were hemispherical with a contact angle of $\sim 45^\circ$ in contrast to the superhydrophilic laser-treated surface, in which the water quickly spread as a film upon contact. This allowed the SiO₂ mixture to be evenly distributed on the SS via a drop-coating method. After drying at room temperature, it possessed high solar reflectivity and mid-infrared emissivity. Next, graphene was induced by the femtosecond laser at high power. The Raman spectra showed three major peaks, D, G, and 2D, at around 1350, 1580, and 2700 cm⁻¹, respectively (Figure S2), and indicated successful LIG preparation.

First, the morphology of the SS was characterized. The low-power femtosecond laser ablation to the UTPI produced coral-like structures with superhydrophilic properties (Figures S3–S5). Consistent with Wenzel's theorem^{53,54}

$$\cos \theta = R_f \cos \theta_0 \quad (1)$$

where θ and θ_0 represent the contact angles on the rough and flat surfaces, respectively, and R_f denotes the roughness factor, which is associated with the ratio of the surface area to its projected area. This equation implies that an increasing roughness factor contributes to the wettability of hydrophilic surfaces. At lower laser powers, the energy input is relatively low, and the effect on the material surface is milder. The modification of the wettability is mainly through the construction of micro- and nanostructures to change the surface properties.

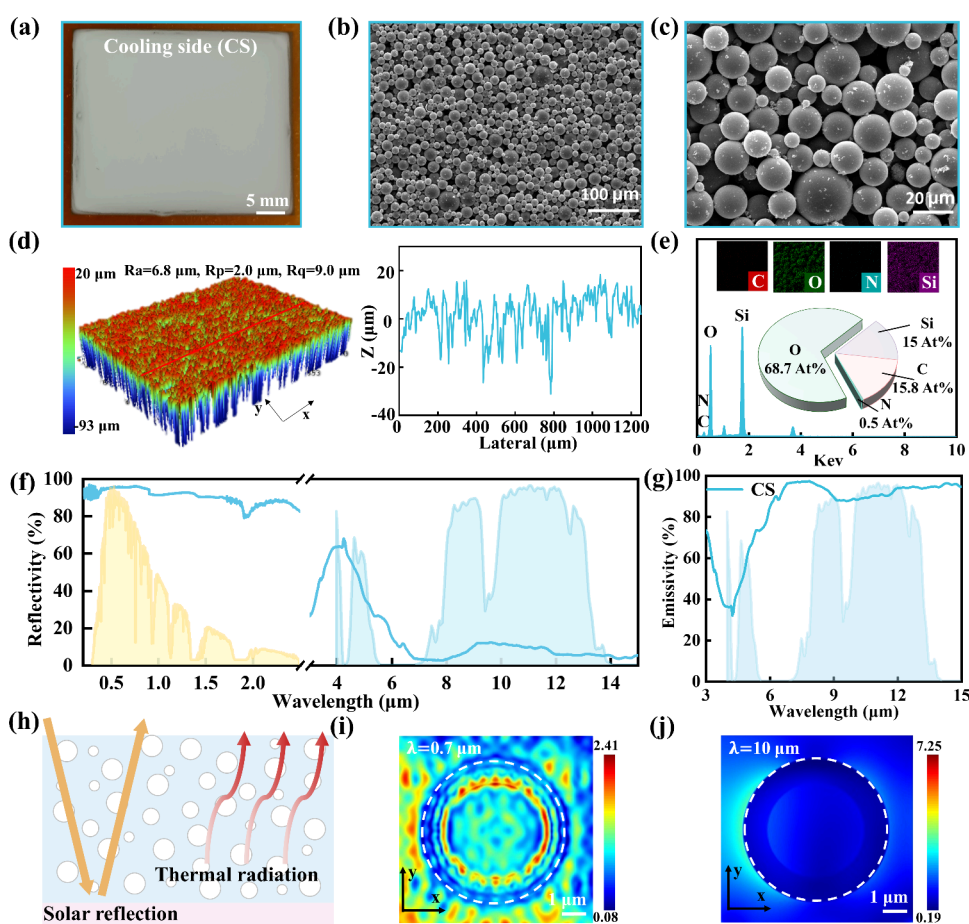


Figure 2. (a–c) Photograph and surface SEM images of dual-mode film showing its cooling side. (d) Three-dimensional morphology and cross-section height of CS. (e) Elemental chemical composition and maps of C, O, N, and Si for CS. (f and g) Solar and mid-infrared emissivity spectra, respectively, of the cooling surface. (h) Schematic showing the CS surface with high solar reflectance and infrared emissivity. (i and j) Diagram of the electromagnetic field strength of SiO₂ at different wavelengths.

Next, the morphology, reflectivity, and emissivity of the CS surface were investigated. Figure 2a shows an optical picture of the dual-mode radiative cooling material. The SiO₂ mixture containing a styrene–butadiene rubber emulsion (SBR) liquid and sodium carboxymethyl cellulose (CMCNa) as a thickener is applied to the superhydrophilic surface and dries to a white color, which is conducive to reflecting sunlight. According to Mie's theory, matching the structure size to the wavelength enhances reflectivity.^{55,56} In the scanning electron microscopy (SEM) images, one can see that the sizes of the hollow SiO₂ microspheres are concentrated within the range of 0.2–20 μm (Figure 2b,c and Figure S6). This size distribution is advantageous for enhancing solar reflectance and achieving high infrared emissivity. The 3D morphology measurements indicated that the surface was rough with most of the bumps on the CS ~ 10–20 μm (Figure 2d). Meanwhile, the chemical element map showed that the content of oxygen and silicon elements increased significantly after the cooling coating was overlaid on the SS and showed that the PI film was completely covered (Figure 2e and Figure S7). It is noteworthy that the solar reflectance on the cooling side of the dual-mode film reached 93% due to the strong solar scattering from the hollow microspheres (Figure 2f). Meanwhile, the high spectral emissivity in the “atmospheric window” is crucial for effective radiative cooling, and the ϵ_{IR} reached about 97% (Figure 2g,h). Next, we employed the finite difference time domain (FDTD)

to calculate the electric field distribution of SiO₂ hollow microspheres with a diameter of 6 μm at wavelengths of 0.7 and 10 μm. These SiO₂ hollow microspheres play an important role in emitting thermal radiation and scattering visible light strongly. A stronger dispersion of the electric field distribution in the visible region was seen.

LIG has been shown to be a favorable solar absorber material. Graphene was induced on the surface of the UTPI film by femtosecond laser line-by-line scanning technology. At high powers, the laser causes carbonization, converting the PI into graphene, which is highly conductive and absorptive. Figure 3a shows an optical photograph of the HS of the dual-mode membrane, and the black color of the LIG indicated favorable light absorption properties. The morphology of the HS was characterized by SEM as shown in panels b and c of Figure 3. The HS surface was extremely rough compared with the flat UTPI film (Figure S8), with regular grooves produced by the femtosecond laser line-by-line scanning technique. These grooves enhance solar light absorption because the deep pores and bumps cause any reflections of sunlight to be absorbed into the material. The height of the irregular bump structure of the LIG was in the range of 20–40 μm (Figure 3d). Energy dispersive spectrometry (EDS) analysis and elemental maps of the HS show a significant increase in the content of C as compared to the UTPI film and SS (Figure 3e and Figure S9), caused by the carbonization of the PI film.

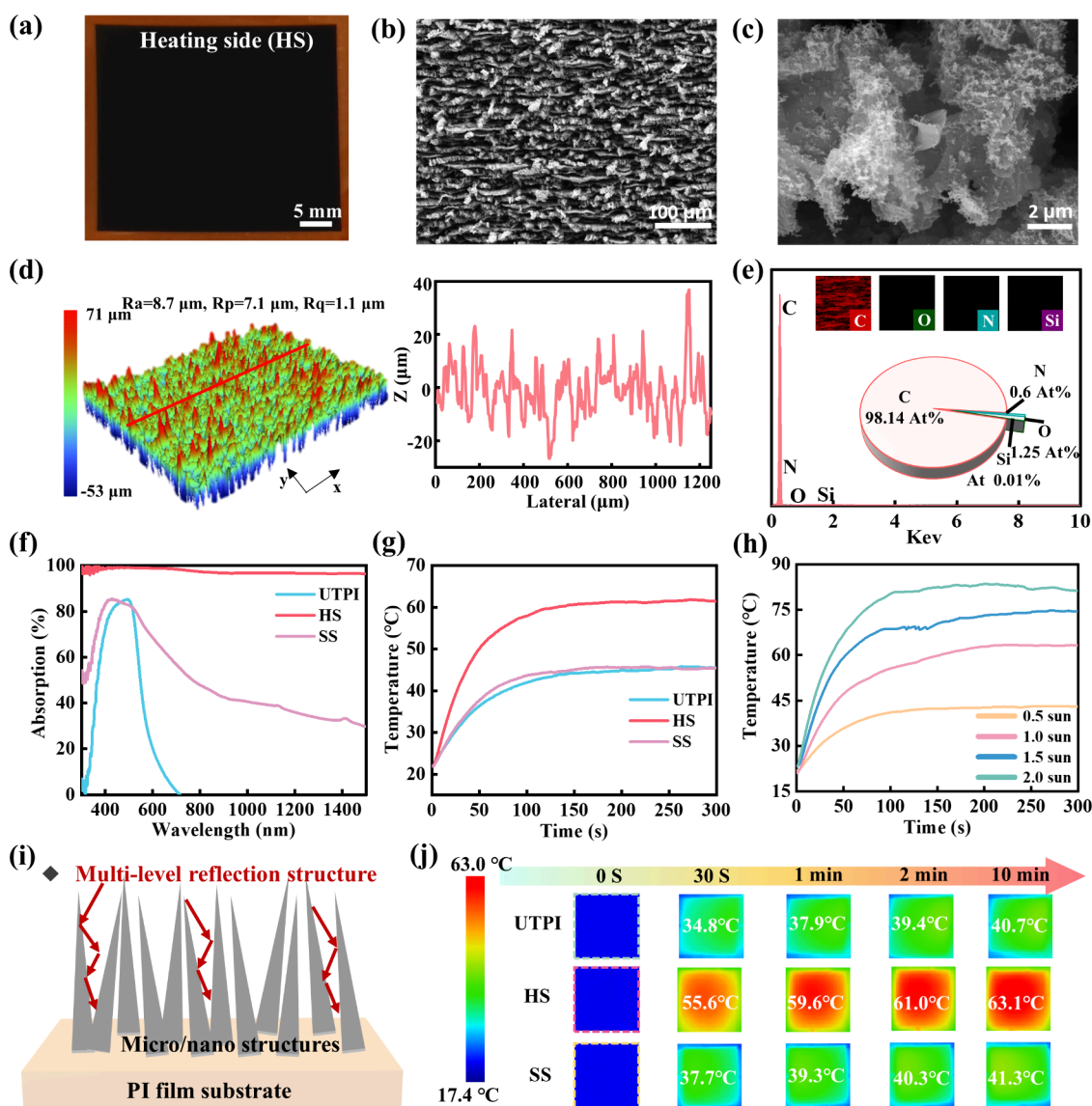


Figure 3. (a) Photograph of the HS of the dual-mode film. (b and c) SEM images of the HS at different magnifications. (d) Three-dimensional morphology and cross-section height of the HS. (e) Elemental chemical composition and maps of C, O, N, and Si for the HS. (f) Solar absorption spectra of the UTPI, HS, and SS. (g) Temperature profiles of the UTPI, HS, and SS under a power of 1.0 kW m^{-2} . (h) Temperature profiles of solar heating materials under solar irradiation intensities of 0.5, 1.0, 1.5, and 2.0 kW m^{-2} . (i) Schematic illustration of solar reflection at heated surface structures. (j) Infrared images of the UTPI, HS, and SS under a power of 1 kW m^{-2} over time.

Subsequently, we systematically investigated the solar heating performance of the UTPI, SS, and HS under different solar irradiation intensities. The broadband absorption of these three samples was first characterized using a visible–near-infrared spectrometer (Figure 3f). Due to the appropriate scanning speed, regular groove structures are formed on the surface of the PI film to further enhance the solar energy absorption and improve the heating performance. The HS showed the highest absorption, reaching 97% because of the black, rough structure of LIG. A solar simulator was applied to simulate a 1 solar irradiation intensity (1 kW m^{-2}), and an infrared camera was used to record the surface temperature of the samples over time. The experimental setup is shown in Figure S10. Generally, the photothermal properties can be quantified by the increase in temperature from ambient temperature to the equilibrium temperature at the sample surface. As shown in Figure 3g, the HS was heated from $22 \text{ }^\circ\text{C}$ ($\Delta T = 40 \text{ }^\circ\text{C}$) in 100 s. At the same time, the

temperature of the UTPI and SS only increased by $23 \text{ }^\circ\text{C}$. To explore the relationship between sun irradiation intensities and the rate of warming, the temperature of the HS at different light intensities was recorded. It can be clearly noted that the maximum temperature and the rate of temperature increase (slope of the curve) are highly dependent on the light intensity (Figure 3h). Figure 3i shows a schematic diagram of the multiple reflections of sunlight inside the HS structure. As the intensity of the light simulator light irradiation increases, the solar heating temperature increases accordingly. An infrared image of the sample under solar irradiation of 1 kW m^{-2} is shown in Figure 3j.

Outdoor scenarios are diverse, changeable, and unpredictable, requiring thermal management materials to be adaptable to complex environments. As shown in Figure S11, the heating and cooling segments of the dual-mode material are side by side on the same side of the PI film. It can be easily switched between heating and cooling functions with a simple

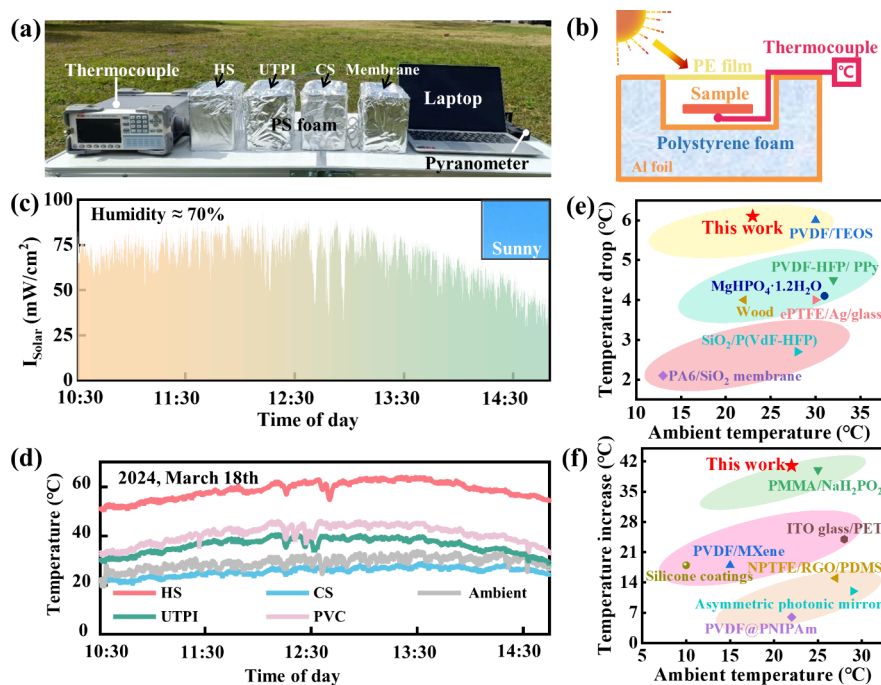


Figure 4. (a) Photograph and (b) schematic showing an experimental device for measuring outdoor cooling and heating performances. Real-time (c) solar irradiance and (d) temperatures of the different samples in Changsha on March 18, 2024. Comparison of (e) the cooling performance of the CS and (f) the heating performance of the HS with other work.

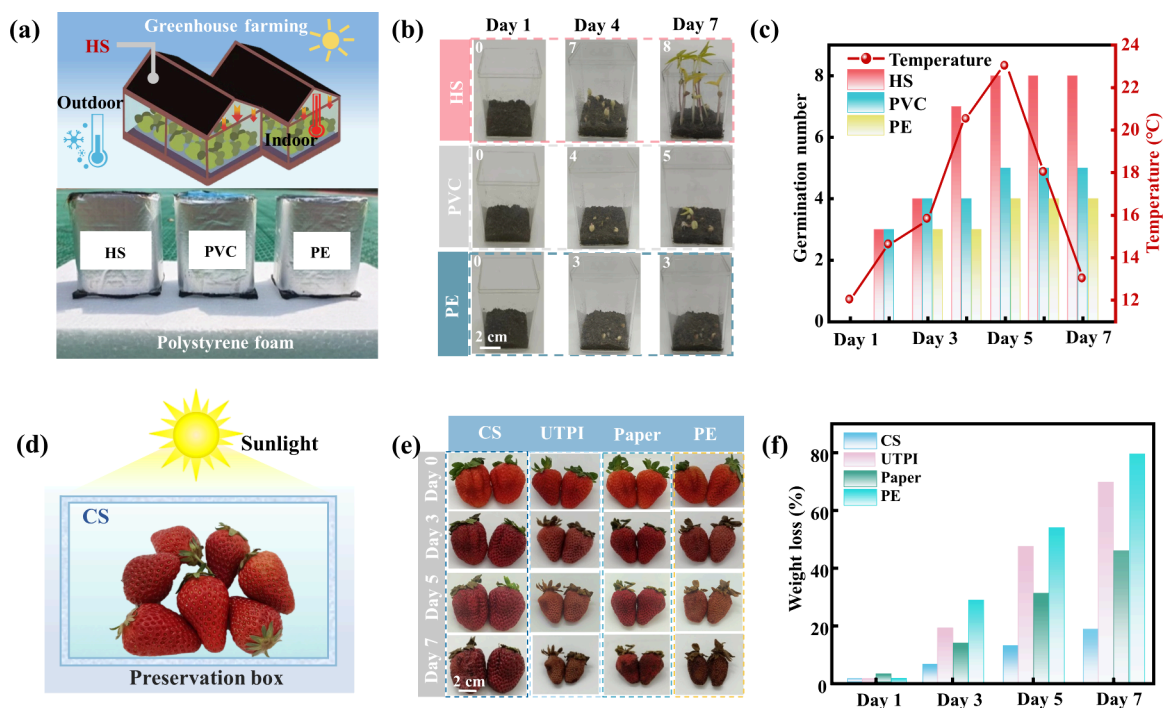


Figure 5. (a) Schematic and digital images of an experiment in an outdoor environment on a sunny day in winter (March 19, 2024, $28^{\circ}11'49''\text{N}$, $112^{\circ}58'42''\text{E}$). (b) Digital images depicting the seed germination progress of the PE, PVC, and HS under sunlight. (c) Number of real-time bean sprouts of the PE, PVC, and HS in continuous experiments (all samples, $\approx 6\text{ cm} \times 6\text{ cm}$; test number, $n = 8$). (d) Schematic of the self-made device for verifying the cooling effects of the CS for fruit preservation. (e) Photographs of the packaged strawberries after storage for 7 days at outer ambient temperature. (f) Effect of different packaging storage methods on weight loss.

mechanical pull-out, expanding its range of outdoor applications. The temperature increase trends of the HS, UTPI, CS, and PVC were investigated under solar radiation intensities of 0.5 and 1 sun equivalent (Figures S12 and S13). It is evident that the HS exhibited the highest temperature and

that a higher solar irradiance resulted in higher temperatures. The SS and PVC displayed similar temperature levels, while the CS consistently maintained the lowest temperature. Panels a and b of Figure 4 show the radiative cooling and heating performance of the HS, UTPI, CS, and membrane exposed to

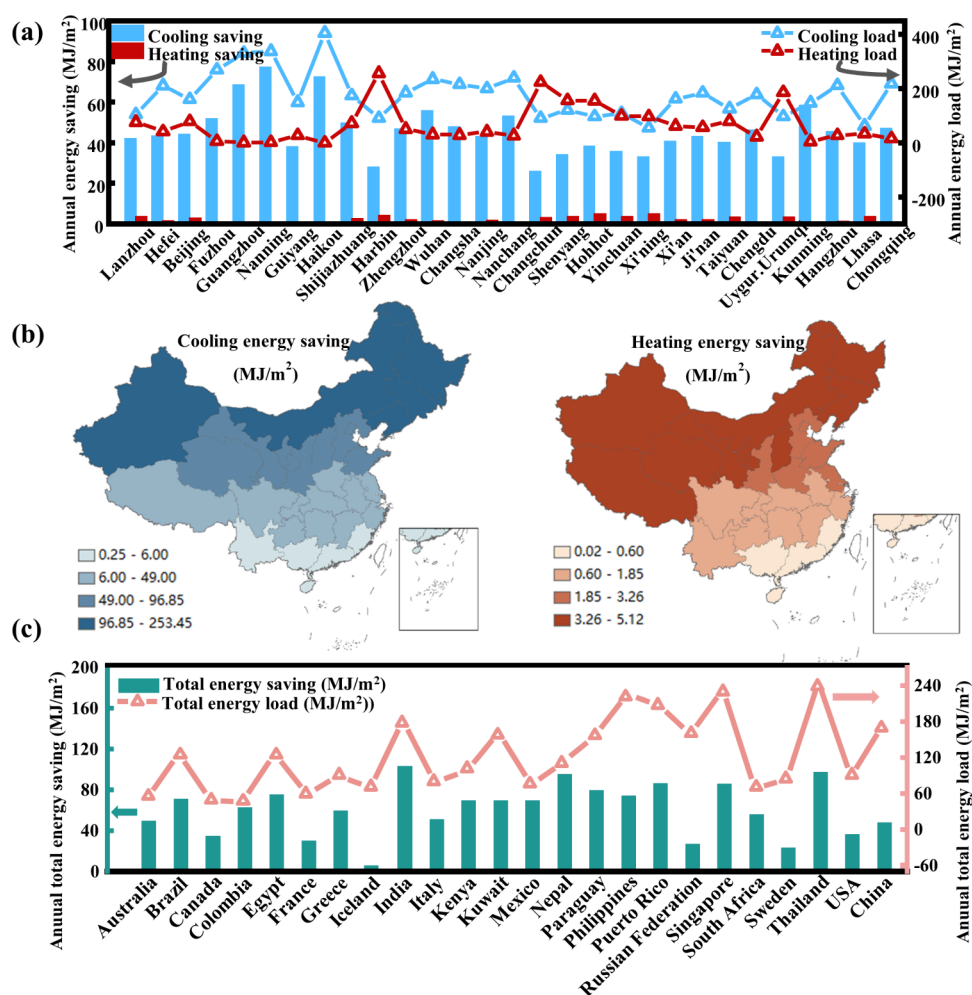


Figure 6. (a) Annual averaged energy savings and loads at different modes over different cities in China. (b) Building energy-saving map for China climate zones. (c) Annual averaged energy savings and loads at different cities around the world.

sunlight. The actual temperature of different materials in the sun is monitored using K-type thermocouples bonded under the surface of the sample. Our experimental apparatus was constructed outdoors on a lawn in Changsha, China (28°11'49"N, 112°58'42"E). The apparatus consisted of polystyrene foam to isolate the samples from the surrounding heat, aluminum foil to reflect the sunlight, and a PE film on the top to reduce heat convection. The solar power densities and experimental results for 4.5 h in a winter environment are shown in panels c and d of Figure 4. The ambient temperature remained above 23 °C during the continuous test with unobstructed sunlight. Compared to the ambient temperature, the CS temperature was reduced by about 6.3 °C under a solar illumination of 75 mW cm⁻² at 12:45–13:15 due to high solar reflectance and high infrared emissivity. The average temperature decrease for other time periods such as 11:00 to 12:00 is 3.8 °C and from 13:30 to 14:30 is 5.3 °C. The average temperature decrease for the whole measurement time was 3.8 °C. Conversely, the temperature of the HS increased by as much as 35 °C under solar irradiation, which can be attributed to its high absorbance and effective photothermal conversion. Temperatures keep on varying mainly affected by factors such as cloud thickness, wind speed, humidity, and angle of solar radiation. The depression of the solar intensity curve corresponded to when cloud cover obstructed the sun. In addition, the temperature of the film responded sensitively to

fluctuations in solar intensity, especially on the HS where the solar absorption is high. Under these winter conditions, the prepared films could still achieve a solar ambient cooling temperature of approximately 6.3 °C and a heating temperature of about 35 °C. Notably, the prepared sample shows superior thermal management performance compared to representative materials reported in the literature (Figure 4e,f and Tables S1 and S2). Therefore, this dual-mode film shows considerable potential for heating and cooling in complex and variable outdoor environments.

We further demonstrated the space thermoregulation capabilities of HS in an agricultural seed germination application since the proper temperature is a key factor that can significantly promote germination. An outdoor bean sprout simulation was developed and tested on a sunny winter day. Three acrylic boxes each containing eight mung bean seeds were wrapped with insulating cotton as a container for seed germination, and PVC, PE, and HS films were incorporated into each of the three boxes to create an artificial greenhouse (Figure 5a). To assess the growth of bean sprouts in the control group outdoors, the number of germinated shoots was quantitatively recorded, as shown in Figure 5b. In our experiment, there were three, four, and seven germinated seeds in the PVC, PE, and HS systems, respectively, after 4 days and three, five, and eight germinated seeds, respectively, after 7 days (Figure 5c), showing that the HS system was

effective in improving the germination of the mung bean. Figure S14 clearly shows that the germinated seedlings in the PVC and PE systems grew at a reduced rate. The reduced temperature in the two systems was suboptimal for the growth of bean sprouts. It has been reported in previous work that the effect of light on the germination of bean sprouts is insignificant at specific temperatures. The outdoor temperature during the experimental period was 12–24 °C and was mostly maintained at around 14 °C. Specifically, the height of bean sprouts measured in the HS system was up to 12 cm on day 7 (Figure S15), in contrast to the height of bean sprouts in the PVC system, which did not exceed 3 cm. The soil itself has some thermal insulation capacity, which can lead to seed germination at these cooler temperatures. However, the temperature of the PVC system did not favor further growth. Similarly, the bean sprouts of the PE system merely germinated, breaking through the soil, but did not continue to grow.

To demonstrate the cooling effects of the CS in a food preservation application, we conducted small-scale experiments using customized equipment, as depicted in Figure Sd. According to the method described by Li et al., thick styrofoam was used as an insulating material and four identical cavities were created inside (6 cm × 8 cm × 6 cm).⁵⁷ In addition, the surface of the styrofoam was covered with aluminum foil with a highly reflective ability for isolation from other environmental factors. Strawberries were selected to evaluate how the different materials affected the freshness of the fruit. The test environment was in Changsha, China, during a sunny summer day between July 3 and 9, 2024. Strawberries were stored within insulated cavities with the openings covered by various films. The fruits were subsequently photographed, and weight loss was recorded over time. Gradual moisture loss and decay of strawberry fruits during storage were found, as shown in Figure Se. The CS has good radiative cooling properties, which can reduce the internal temperature inside the package and slow the metabolic and physiological aging of strawberries. Specifically, strawberries covered with CS exhibited the slowest volume change, in comparison to those covered with the UTPI, PE, and paper. The weight loss rate serves as a critical indicator for evaluating the effectiveness of freshness preservation. Figure Sf shows the weight loss rate of strawberries over 7 days. Furthermore, the weight loss rates of all three sets increased over time. Notably, the PE and UTPI sets displayed the highest weight loss rate due to the rapid water loss of the strawberries. Moreover, the weight loss rate of the strawberries in the paper system is about half of that in the PE system. Due to the high reflectivity and infrared emissivity of the hollow SiO₂ microspheres, the CS-covered container was more prone to heat transfer to the outdoor atmosphere. The surface temperature of the dual-mode film directly influences the internal temperature of the containers through conductive and radiative heat transfer. The insulating materials used in the experimental setups minimize heat loss to the environment, ensuring that the internal temperature closely follows the surface temperature of the film. In short, the dual-mode thermal management film we prepared demonstrates its potential for application in agricultural development and fruit preservation. The optical properties of the surfaces were also very stable and remained almost unchanged after exposure to outdoor environmental conditions for 30 days (Figure S16).

In order to quantitatively predict the potential impact of our dual-mode devices on building energy efficiency, we used

Energy-plus in conjunction with material performance data to calculate the energy savings of heating-only, cooling-only, and dual-mode building envelopes for a full year, including 29 cities, such as Hefei, Beijing, Fuzhou, Lanzhou, Guangzhou, Nanjing, Haikou, Nanning, and others, selected to represent the 29 climate zones in China. The corresponding cooling-only and heating-only energy savings data and load maps are shown in panels a and b, respectively, of Figure 6. First, we observe that solar heating is more favorable in the north, while radiant cooling is more favorable in the south, which was expected because of the dependence of the climate on latitude. In general, the higher the temperature of an object, the more pronounced the radiative cooling effect. Second, radiant cooling energy savings are greater than solar heating energy savings. This can be attributed to the fact that the hot summer climate in many regions drives higher summer energy consumption, while winters generally see less extreme temperatures, resulting in lower heating requirements. It is worth noting that the simulations show that the combination of the dual functions allows them to achieve significant year-round energy savings in China. Meanwhile, the annual energy saving simulation results for 24 typical cities worldwide (Figure 6c and Figure S17) similarly demonstrate the global applicability of the thermal management capabilities of the prepared samples. The smart thermal management performance of the dual-mode thermal management devices contributes to the optimization of the energy mix in the smart building sector, which is a key strategy that will help achieve “dual-carbon” climate goals.

Energy efficient building solutions with adjustable heating and cooling are crucial in order to address potentially more extreme climate events, which are predicted to have increased frequency and magnitude. In this work, we experimentally demonstrate the heating and cooling performance of a dual-mode building envelope. The prepared dual-mode surface films allow for controllable switching of heating and cooling modes by means of surface substitution. A uniform SiO₂ hollow microsphere coating on a superhydrophilic surface was demonstrated as the cooling side, which effectively reflected sunlight and emitted IR radiation, and exhibited ultrahigh R_{solar} and ϵ_{IR} values of 93% and 97%, respectively. It achieved a solar ambient cooling temperature of ~6.3 °C at a solar density of 75 J/cm². The heating side was graphene induced by a femtosecond laser on polyimide surfaces, which had 97% solar light absorption and allowed efficient photothermal conversion. A superambient heating temperature of 40 °C was achieved under 1 solar intensity. In practice, the dual-mode surfaces provided excellent temperature regulation in exterior environments. Dual-mode films with integrated heating and cooling functions have great potential for various diverse applications and offer new possibilities for building thermal management systems due to their low cost and easy fabrication methods.

■ ASSOCIATED CONTENT

Supporting Information

The Supporting Information is available free of charge at <https://pubs.acs.org/doi/10.1021/acs.jpcllett.5c00436>.

Experimental methods, performance comparison tables, contact angles of the UTPI and SS, Raman spectra, SEM images of the UTPI, SS, CS, and HS, three-dimensional morphology, cross-section height of the SS, optical

photograph of a dual-mode thermal management film, temperatures of the CS, HS, UTPI, and PVC at different solar intensities, images of HS, PVC, and PE seed germination over time, number of seeds germinated in the HS, PVC, and PE over time, reflectivity and absorption spectra of the CS and HS, and annual global energy savings under dual-mode thermal management regulation (PDF)

AUTHOR INFORMATION

Corresponding Author

Kai Yin – Hunan Key Laboratory of Nanophotonics and Devices, School of Physics and State Key Laboratory of Precision Manufacturing for Extreme Service Performance, College of Mechanical and Electrical Engineering, Central South University, Changsha 410083, China; State Key Laboratory of Intelligent Manufacturing Equipment and Technology, Huazhong University of Science and Technology, Wuhan 430000, China; orcid.org/0000-0002-0763-3834; Email: kaiyin@csu.edu.cn

Authors

Tingni Wu – Hunan Key Laboratory of Nanophotonics and Devices, School of Physics, Central South University, Changsha 410083, China

Yuchun He – Hunan Key Laboratory of Nanophotonics and Devices, School of Physics, Central South University, Changsha 410083, China

Lingxiao Wang – Hunan Key Laboratory of Nanophotonics and Devices, School of Physics, Central South University, Changsha 410083, China

Haonan Yu – Hunan Key Laboratory of Nanophotonics and Devices, School of Physics, Central South University, Changsha 410083, China

Yin Huang – Hunan Key Laboratory of Nanophotonics and Devices, School of Physics, Central South University, Changsha 410083, China

Ji-An Duan – State Key Laboratory of Precision Manufacturing for Extreme Service Performance, College of Mechanical and Electrical Engineering, Central South University, Changsha 410083, China; orcid.org/0000-0001-5104-3148

Christopher J. Arnusch – Department of Desalination and Water Treatment, Zuckerberg Institute for Water Research, The Jacob Blaustein Institutes for Desert Research, Ben-Gurion University of the Negev, Midreshet Ben-Gurion 84990, Israel; orcid.org/0000-0002-1462-1081

Complete contact information is available at:

<https://pubs.acs.org/10.1021/acs.jpcllett.5c00436>

Notes

The authors declare no competing financial interest.

ACKNOWLEDGMENTS

This research was supported by the National Natural Science Foundation of China (Grants 52475499, 52222513, and 52075557), the National Key R&D Program of China (2023YFB4604200), the Natural Science Foundation of Hunan Province (Grant 2024JJ5426), the Central South University Innovation-Driven Research Program (Grant 2023CXQD019), the State Key Laboratory of Precision Manufacturing for Extreme Service Performance, Central

South University (ZZYJKT2023-12), the State Key Laboratory of Intelligent Manufacturing Equipment and Technology, Huazhong University of Science and Technology (IM-ETKF2024018), and the Fundamental Research Funds for the Central Universities of Central South University (Grants 2024ZZTS0015 and 2025ZZTS0681).

REFERENCES

- (1) Zhang, Q.; Wang, Y.; Lv, Y.; Yu, S.; Ma, R. Bioinspired zero-energy thermal-management device based on visible and infrared thermochromism for all-season energy saving. *Proc. Natl. Acad. Sci. U. S. A.* **2022**, *119*, No. e2207353119.
- (2) Li, T.; Zhai, Y.; He, S. M.; Gan, W. T.; Wei, Z. Y.; Heidarnejad, M.; Dalgo, D.; Mi, R. Y.; Zhao, X. P.; Song, J. W.; Dai, J. Q.; Chen, C. J.; Aili, A.; Vellore, A.; Martini, A.; Yang, R. G.; Srebric, J.; Yin, X. B.; Hu, L. B. A radiative cooling structural material. *Science* **2019**, *364*, 760–763.
- (3) Yin, X.; Yang, R.; Tan, G.; Fan, S. Terrestrial radiative cooling: Using the cold universe as a renewable and sustainable energy source. *Science* **2020**, *370*, 786–791.
- (4) Chu, S.; Majumdar, A. Opportunities and challenges for a sustainable energy future. *Nature* **2012**, *488*, 294–303.
- (5) Timilsina, G. R.; Kurdgelashvili, L.; Narbel, P. A. Solar energy: Markets, economics and policies. *Renew Sust Energy Rev.* **2012**, *16*, 449–465.
- (6) Wu, X.; Chen, G. Y.; Owens, G.; Chu, D.; Xu, H. Photothermal materials: A key platform enabling highly efficient water evaporation driven by solar energy. *Mater. Today Energy* **2019**, *12*, 277–296.
- (7) Kumar, L.; Ahmed, J.; El Haj Assad, M.; Hasanuzzaman, M. Prospects and challenges of solar thermal for process heating: A Comprehensive Review. *Energies* **2022**, *15*, 8501.
- (8) Ahmed, F. E.; Hashaikeh, R.; Hilal, N. Solar powered desalination - technology, energy and future outlook. *Desalination* **2019**, *453*, 54–76.
- (9) Yang, W.; Xiao, P.; Ni, F.; Zhang, C.; Gu, J.; Kuo, S. W.; Liu, Q.; Chen, T. Biomass-derived nanostructured coatings based on cellulose nanofibers-melanin hybrids toward solar-enabled multifunctional energy management. *Nano Energy* **2022**, *97*, No. 107180.
- (10) Xie, D.; Li, H. H.; Diao, W. Y.; Jiang, R.; Tao, F. Y.; Sun, H. Z.; Wu, X. L.; Zhang, J.-P. Spatial confinement of vertical arrays of lithophilic SnS₂ nanosheets enables conformal Li nucleation/growth towards dendrite-free Li metal anode. *Energy Storage Mater.* **2021**, *36*, 504–513.
- (11) Huang, Z.; Ruan, X. Nanoparticle embedded double-layer coating for daytime radiative cooling. *Int. J. Heat Mass Tran.* **2017**, *104*, 890–896.
- (12) Chen, Z.; Zhu, L.; Raman, A.; Fan, S. Radiative cooling to deep sub-freezing temperatures through a 24-h day-night cycle. *Nat. Commun.* **2016**, *7*, 13729.
- (13) Raman, A. P.; Abou Anoma, M.; Zhu, L.; Rephaeli, E.; Fan, S. Passive radiative cooling below ambient air temperature under direct sunlight. *Nature* **2014**, *515*, 540–544.
- (14) Xue, X.; Qiu, M.; Li, Y.; Zhang, Q. M.; Li, S.; Yang, Z.; Feng, C.; Zhang, W.; Dai, J. G.; Lei, D.; Jin, W.; Xu, L.; Zhang, T.; Qin, J.; Wang, H.; Fan, S. Creating an Eco-Friendly Building Coating with Smart Subambient Radiative Cooling. *Adv. Mater.* **2020**, *32*, 1906751.
- (15) Lee, D.; Go, M.; Son, S.; Kim, M.; Badloe, T.; Lee, H.; Kim, J. K.; Rho, J. Sub-ambient daytime radiative cooling by silica-coated porous anodic aluminum oxide. *Nano Energy* **2021**, *79*, 105426.
- (16) Rephaeli, E.; Raman, A.; Fan, S. Ultrabroadband photonic structures to achieve high-performance daytime radiative cooling. *Nano Lett.* **2013**, *13*, 1457–1461.
- (17) Hossain, M. M.; Jia, B.; Gu, M. A metamaterial emitter for highly efficient radiative cooling. *Adv. Opt. Mater.* **2015**, *3*, 1047–1051.
- (18) Zhu, L.; Raman, A. P.; Fan, S. Radiative cooling of solar absorbers using a visibly transparent photonic crystal thermal blackbody. *Proc. Natl. Acad. Sci. U. S. A.* **2015**, *112*, 12282–12287.

- (19) Zhang, H.; Ly, K. C. S.; Liu, X.; Chen, Z.; Yan, M.; Wu, Z.; Wang, X.; Zheng, Y.; Zhou, H.; Fan, T. Biologically inspired flexible photonic films for efficient passive radiative cooling. *Proc. Natl. Acad. Sci. U. S. A.* **2020**, *117*, 14657–14666.
- (20) Gentle, A. R.; Smith, G. B. A subambient open roof surface under the mid-summer sun. *Adv. Sci.* **2015**, *2*, 1500119.
- (21) Lin, C.; Li, Y.; Chi, C.; Kwon, Y. S.; Huang, J.; Wu, Z.; Zheng, J.; Liu, G.; Tso, C. Y.; Chao, C. Y. H.; Huang, B. A solution-processed inorganic emitter with high spectral selectivity for efficient subambient radiative cooling in hot humid climates. *Adv. Mater.* **2022**, *34*, 2109350.
- (22) Zhang, L.; Luo, B.; Fu, K.; Gao, C.; Han, X.; Zhou, M.; Zhang, T.; Zhong, L.; Hou, Y.; Zheng, Y. Highly efficient photothermal icephobic/de-icing MOF-based micro and nanostructured surface. *Adv. Sci.* **2023**, *10*, 2304187.
- (23) Goldstein, E. A.; Raman, A. P.; Fan, S. Sub-ambient non-evaporative fluid cooling with the sky. *Nat. Energy* **2017**, *2*, 17143.
- (24) Mandal, J.; Fu, Y.; Overvig, A. C.; Jia, M.; Sun, K.; Shi, N. N.; Zhou, H.; Xiao, X.; Yu, N.; Yang, Y. Hierarchically porous polymer coatings for highly efficient passive daytime radiative cooling. *Science* **2018**, *362*, 315–318.
- (25) Shi, N. N.; Tsai, C. C.; Camino, F.; Bernard, G. D.; Yu, N.; Wehner, R. Keeping cool: enhanced optical reflection and radiative heat dissipation in Saharan silver ants. *Science* **2015**, *349*, 298–301.
- (26) Hsu, P. C.; Song, A. Y.; Catrysse, P. B.; Liu, C.; Peng, Y.; Xie, J.; Fan, S.; Cui, Y. Radiative human body cooling by nanoporous polyethylene textile. *Science* **2016**, *353*, 1019–1023.
- (27) Hsu, P. C.; Liu, C.; Song, A. Y.; Zhang, Z.; Peng, Y.; Xie, J.; Liu, K.; Wu, C. L.; Catrysse, P. B.; Cai, L.; Zhai, S.; Majumdar, A.; Fan, S.; Cui, Y. A dual-mode textile for human body radiative heating and cooling. *Sci. Adv.* **2017**, *3*, 1700895.
- (28) Zhai, Y.; Ma, Y.; David, S. N.; Zhao, D.; Lou, R.; Tan, G.; Yang, R.; Yin, X. Scalable-manufactured randomized glass-polymer hybrid metamaterial for daytime radiative cooling. *Science* **2017**, *355*, 1062–1066.
- (29) Bhatia, B.; Leroy, A.; Shen, Y.; Zhao, L.; Gianello, M.; Li, D.; Gu, T.; Hu, J.; Soljacic, M.; Wang, E. N. Passive directional sub-ambient daytime radiative cooling. *Nat. Commun.* **2018**, *9*, 5001.
- (30) Zhao, D.; Aili, A.; Zhai, Y.; Lu, J.; Kidd, D.; Tan, G.; Yin, X.; Yang, R. Subambient cooling of water: toward real-world applications of daytime radiative cooling. *Joule* **2019**, *3*, 111–123.
- (31) Fan, S.; Raman, A. Metamaterials for radiative sky cooling. *National Science Review* **2018**, *5*, 132–133.
- (32) Li, W.; Shi, Y.; Chen, Z.; Fan, S. Photonic thermal management of coloured objects. *Nat. Commun.* **2018**, *9*, 4240.
- (33) Shi, N. N.; Tsai, C. C.; Carter, M. J.; Mandal, J.; Overvig, A. C.; Sfeir, M. Y.; Lu, M.; Craig, C. L.; Bernard, G. D.; Yang, Y.; Yu, N. Nanostructured fibers as a versatile photonic platform: radiative cooling and waveguiding through transverse Anderson localization. *Light: Sci. Appl.* **2018**, *7*, 37.
- (34) Hong, S.; Gu, Y.; Seo, J. K.; Wang, J.; Liu, P.; Meng, Y. S.; Xu, S.; Chen, R. Wearable thermoelectrics for personalized thermoregulation. *Sci. Adv.* **2019**, *5*, No. eaaw0536.
- (35) Zhang, X. A.; Yu, S.; Xu, B.; Li, M.; Peng, Z.; Wang, Y.; Deng, S.; Wu, X.; Wu, Z.; Ouyang, M.; Wang, Y. Dynamic gating of infrared radiation in a textile. *Science* **2019**, *363*, 619–623.
- (36) Zhou, L.; Song, H.; Liang, J.; Singer, M.; Zhou, M.; Stegenburgs, E.; Zhang, N.; Xu, C.; Ng, T.; Yu, Z.; Ooi, B.; Gan, Q. A polydimethylsiloxane-coated metal structure for all-day radiative cooling. *Nat. Sustain.* **2019**, *2*, 718–724.
- (37) Wang, W.; Zou, Q.; Wang, N.; Hong, B.; Zhang, W.; Wang, G. P. Janus multilayer for radiative cooling and heating in double-side photonic thermal system. *ACS Appl. Mater. Interfaces* **2021**, *13*, 42813–42821.
- (38) Miao, D.; Cheng, N.; Wang, X.; Yu, J.; Ding, B. Integration of janus wettability and heat conduction in hierarchically designed textiles for all-day personal radiative cooling. *Nano Lett.* **2022**, *22*, 680–687.
- (39) Ji, X.; Jiang, Y.; Liu, T.; Lin, S.; Du, A. MXene aerogel-based phase change film for synergistic thermal management inspired by antifreeze beetles. *Cell Rep. Phys. Sci.* **2022**, *3*, No. 100815.
- (40) Yue, X.; Zhang, T.; Yang, D.; Qiu, F.; Wei, G.; Zhou, H. Multifunctional Janus fibrous hybrid membranes with sandwich structure for on-demand personal thermal management. *Nano Energy* **2019**, *63*, No. 103808.
- (41) Yue, X.; Zhang, T.; Yang, D.; Qiu, F.; Wei, G.; Lv, Y. A robust Janus fibrous membrane with switchable infrared radiation properties for potential building thermal management applications. *J. Mater. Chem. A* **2019**, *7*, 8344–8352.
- (42) Wu, J.; He, J.; Yin, K.; Zhu, Z.; Xiao, S.; Wu, Z.; Duan, J. Robust hierarchical porous PTFE film fabricated via femtosecond laser for self-cleaning passive cooling. *Nano Lett.* **2021**, *21*, 4209–4216.
- (43) He, Y.; Yin, K.; Wang, L.; Wu, T.; Chen, Y.; Arnusch, C. J. Femtosecond laser structured black superhydrophobic cork for efficient solar-driven cleanup of crude oil. *Appl. Phys. Lett.* **2024**, *124*, No. 171601.
- (44) Wu, Z.; Yin, K.; Wu, J.; Zhu, Z.; Duan, J. A.; He, J. Recent advances in femtosecond laser-structured Janus membranes with asymmetric surface wettability. *Nanoscale* **2021**, *13*, 2209–2226.
- (45) Cheng, K.; Xu, W.; Wu, H.; Chen, B.; Yang, H.; Cui, Z.; Yu, H.; Cheng, Z.; Hu, Y.; Li, J.; Jiang, H.; Chu, J.; Wu, D. Light-Triggered Droplet Gating Strategy Based on Janus Membrane Fabricated by Femtosecond Laser. *ACS Nano* **2024**, *18*, 32481–32490.
- (46) Wu, T.; Yin, K.; Pei, J.; He, Y.; Duan, J. A.; Arnusch, C. J. Femtosecond laser-textured superhydrophilic coral-like structures spread AgNWs enable strong thermal camouflage and anti-counterfeiting. *Appl. Phys. Lett.* **2024**, *124*, No. 161602.
- (47) Deng, Q.; Wu, T.; Yin, K.; Li, X.; Wang, L.; Huang, Q.; Huang, Y.; Arnusch, C. J.; Duan, J. A. Efficient anti-frosting enabled by femtosecond laser-induced salt-philic and superhydrophobic surface. *Appl. Phys. Lett.* **2024**, *125*, No. 121602.
- (48) Yang, P.; Yin, K.; Li, X.; Song, X.; Wang, L.; Pei, J.; Wu, T.; Huang, Y.; Awan, S. U.; Khalil, A. S. G. Domino-like water film manipulation with multifunctionality. *Appl. Phys. Lett.* **2024**, *125*, No. 051602.
- (49) Wu, T.; Wu, Z.; He, Y.; Zhu, Z.; Wang, L.; Yin, K. Femtosecond laser textured porous nanowire structured glass for enhanced thermal imaging. *Chin. Opt. Lett.* **2022**, *20*, No. 033801.
- (50) Pei, J.; Yin, K.; Wu, T.; Wang, L.; Deng, Q.; Huang, Y.; Wang, K.; Arnusch, C. J. Multifunctional polyimide-based femtosecond laser micro/nanostructured films with triple Janus properties. *Nanoscale* **2023**, *15*, 15708–15716.
- (51) Yin, K.; Wu, Z.; Wu, J.; Zhu, Z.; Zhang, F.; Duan, J. A. Solar-driven thermal-wind synergistic effect on laser-textured superhydrophilic copper foam architectures for ultrahigh efficient vapor generation. *Appl. Phys. Lett.* **2021**, *118*, No. 211905.
- (52) Huang, Q.; Yin, K.; Wang, L.; Deng, Q.; Arnusch, C. J. Femtosecond laser-scribed superhydrophilic/superhydrophobic self-splitting patterns for one droplet multi-detection. *Nanoscale* **2023**, *15*, No. 11247.
- (53) Bell, M. S.; Borhan, A. A volume-corrected Wenzel model. *ACS Omega* **2020**, *5*, 8875–8884.
- (54) Wu, T.; Yin, K.; Zhang, H.; Wang, L.; He, Y.; He, J.; Duan, J. A.; Arnusch, C. J. Water-triggered visible and infrared light reversible switch using nanowires-covered micropores superhydrophilic surfaces. *Chem. Eng. J.* **2023**, *461*, No. 141894.
- (55) Ding, Z.; Li, X.; Ji, Q.; Zhang, Y.; Li, H.; Zhang, H.; Pattelli, L.; Li, Y.; Xu, H.; Zhao, J. Machine-learning-assisted design of a robust biomimetic radiative cooling metamaterial. *ACS Mater. Lett.* **2024**, *6*, 2416–2424.
- (56) Ding, Z.; Pattelli, L.; Xu, H.; Sun, W.; Li, X.; Pan, L.; Zhao, J.; Wang, C.; Zhang, X.; Song, Y.; Qiu, J.; Li, Y.; Yang, R. Iridescent daytime radiative cooling with no absorption peaks in the visible range. *Small* **2022**, *18*, 2202400.

(57) Li, J.; Liang, Y.; Li, W.; Xu, N.; Zhu, B.; Wu, Z.; Wang, X.; Fan, S.; Wang, M.; Zhu, J. Protecting ice from melting under sunlight via radiative cooling. *Sci. Adv.* **2022**, *8*, No. eabj9756.